ISSN: 2710-0588

Prediction and Nonlinear Analysis of Dynamic Gas Foil Bearing-High-Speed Rotor System

Huan Zhao[1], Teng Hu[1,2], Sijia Peng[1], Zichun Ma[1], Hualin Zheng[1]

[1] School of Mechatronic Engineering, Southwest Petroleum University, Chengdu, Sichuan 610500, China

[2] Sichuan Provincial Science and Technology Resource Sharing Service Platform for Oil and Gas Equipment Technology, Chengdu, Sichuan 610500, China

Abstract

To address the instability problem of foil-driven hydrodynamic gas bearing-rotor systems in high-speed oil-free rotating machinery, this paper establishes a high-fidelity transient multi-field coupled dynamic prediction model. The core of this model is that it skips the traditional linear stiffness/damping simplification and directly obtains the transient film force by solving the unsteady Reynolds equations that account for the squeezing effect. The paper details the numerical process of solving the transient flow field using the Alternating Direction Implicit (ADI) method and integrates it with the Timoshenko beam finite element rotor model. The transient response of the rotor under aeroelastic coupling effect is simulated using the prediction-correction multi-field coupled trajectory method. The bifurcation evolution law of the system over a wide speed range is investigated in detail. The study finds that after exceeding the critical speed of 14000 r/min, the system undergoes Hopf bifurcation induced by instability at the equilibrium point, subsequently evolving into a limit cycle motion with significant subsynchronous characteristics. With further increases in speed, the subsynchronous eddy frequency ratio evolves from 0.5X to 0.21X, revealing the frequency modulation mechanism caused by the nonlinear film force.

Keywords

Dynamic Gas Bearings, ADI Algorithm, Nonlinear Dynamics, Fluid-Structure Interaction.

1. Introduction

Rotating machinery plays an indispensable role in aerospace, precision engineering and new energy fields[1]. As equipment develops towards ultra-high speed and high power density, extremely stringent requirements are placed on the operational stability of the support bearings. The foil dynamic pressure gas bearing consists of a flat foil, a corrugated foil and a bearing housing, as shown in Figure 1. During high-speed rotation, a wedge-shaped gap is formed between the rotor and the flat foil, generating a dynamic pressure gas film, while the corrugated elastic corrugated foil at the bottom provides structural stiffness and Coulomb friction damping for the system. Since Blok and Van Rossum[2] first proposed the concept of foil bearings in 1953, they have been widely used in oil-free air circulators, compressors and other equipment.

Despite the significant advantages of GFB, the compressibility of the gas and the low stiffness and low damping characteristics of the gas film make the rotor prone to instability during high-speed operation. Kim and San Andrés et al.[3][4]conducted a systematic study on the static and dynamic thermo-elastic-hydrodynamics of foil bearings, pointing out that the increase in temperature will cause changes in the bearing stiffness and damping coefficient. In China, Yu Lie et al.[5][6]predicted the performance of foil bearings through aeroelastic coupling solution;

ISSN: 2710-0588

Xu Huaijin et al.[7][8]used the perturbation method to analyze the influence of structural parameters on dynamic characteristic coefficients. However, it is still a challenge for the engineering community to perform high-precision real-time transient coupling solution of the unsteady gas lubrication Reynolds equation and the motion equation of the multi-degree-of-freedom flexible rotor, and to fully reveal the nonlinear characteristics such as bifurcation and chaos of the system. This paper conducts an in-depth analysis of the nonlinear dynamic behavior of the high-speed radial gas bearing-rotor system by establishing an accurate multi-physics coupled trajectory prediction model.

Figure 1. Foil hydrodynamic gas bearing

2. Coupled Modeling of Transient Flow Field and Rotor System

As is well known, the rotor dynamics equations describing rotor motion are ordinary differential equations, while the transient gas lubrication Reynolds equations describing gas lubrication are partial differential equations. Therefore, the coupled dynamics problem of the gas bearing-rotor system is a multi-physics coupled problem, and its solution necessarily involves the coupled problem of solving two types of equations. This section studies the coupling effect between rotor motion and gas lubrication film flow field, and then analyzes its coupled dynamic characteristics.

2.1. Transient Reynolds Equation Model for Gas Lubrication of Foil Gas Dynamic Bearing

In the transient Reynolds equation, the $\frac{\partial(ph)}{\partial t}$ term is the squeezing effect term, which is closely related to the rotor's motion. When analyzing static characteristics, the squeezing effect term can be ignored; however, when analyzing the dynamics of a gas bearing-rotor coupled system, this squeezing effect term must be considered. Therefore, this section focuses on the gas lubrication film characteristics considering the gas squeezing effect term (i.e., the time term), obtaining a gas dynamics equation describing the physical properties, laying the foundation for the dynamic analysis of the gas bearing-rotor coupled system.

For a purely hydrodynamic radial gas bearing, neglecting the flow in the Z direction, its gas lubrication transient Reynolds equation is shown in equation (1):

$$\frac{\partial}{\partial x}\left(h^3 p\frac{\partial p}{\partial x}\right)+\frac{\partial}{\partial z}\left(h^3 p\frac{\partial p}{\partial z}\right)=6\mu V_{x1}\frac{\partial}{\partial x}(ph)+12\mu\frac{\partial(ph)}{\partial t} \tag{1}$$

Transforming to a cylindrical coordinate system, let x = Rθ, and assuming no slippage between the fluid and the rotor surface, i.e., Vx1 = Rω, substituting into the above equation, we get:

ISSN: 2710-0588

$$-\frac{\partial}{\partial\theta}\left(ph^3\frac{\partial p}{\partial\theta}\right)-R^2\frac{\partial}{\partial z}\left(ph^3\frac{\partial p}{\partial z}\right)+6\mu\omega R^2\frac{\partial}{\partial\theta}(ph)+12R^2\mu\frac{\partial(ph)}{\partial t}=0 \tag{2}$$

Dimensionless parameters are used:

$$\xi=\frac{z}{R},\bar{p}=\frac{p}{p_a},\bar{h}=\frac{h}{h_m},\Lambda=\frac{6\mu\omega R^2}{p_a h_m^2},\tau=\frac{\omega t}{2\Lambda} \tag{3}$$

The dimensionless transient Reynolds equation for gas lubrication can be obtained as follows:

$$-\frac{\partial}{\partial\theta}\left(\bar{p}\bar{h}^3\frac{\partial\bar{p}}{\partial\theta}\right)-\frac{\partial}{\partial\xi}\left(\bar{p}\bar{h}^3\frac{\partial\bar{p}}{\partial\xi}\right)+\Lambda\frac{\partial}{\partial\theta}(\bar{p}\bar{h})+\frac{\partial(\bar{p}\bar{h})}{\partial\tau}=0 \tag{4}$$

2.2. Numerical Analysis Method for Transient Gas Lubrication Reynolds Equation based on ADI Method

For the partial differential equation (4) in the previous section, the implicit variable direction method (ADI) is used for solution. The central difference method is used to discretize the directions θ and ξ. The entire process uses a normalized grid. The specific solution domain is shown in Figure 2. The computational domain is $\theta(0:NX+1)$ and $\xi(0:NZ+1)$, and the solution domain is $\theta(1:NX)$ and $\xi(1:NZ)$. The boundary conditions are as follows: atmospheric boundary condition is $p(\xi=0)=p(\xi=NZ)=p_a$; periodic boundary conditions are $p(\theta=0)=p(\theta=NX)$ and $p(\theta=1)=p(\theta=NX+1)$.

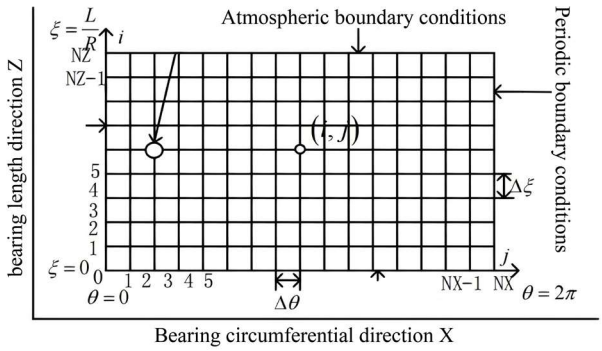

Figure 2. Schematic diagram of the computational domain for gas bearings

For the time term in equation (4), the implicit method with variable direction is used to discretize it. The specific process is as follows: The time process is divided into three discrete time periods: n, n+1 and n+2 for solution. The time difference between the two adjacent periods is the dimensionless time Δτ. Each iteration cycle step includes two processes: solving the n+1 step and solving the n+2 step. In the initial calculation process, it is assumed that the pressure distribution in the nth step is known. In the process of solving the first step of the iteration cycle, i.e., the n+1 step, the partial derivative with respect to the θ direction is used as the unknown parameter, and the partial derivative with respect to the ξ direction is used as the known parameter obtained from the nth step; in the process of solving the next step of the iteration cycle, i.e., the n+2 step, the partial derivative with respect to the ξ direction is used as the unknown parameter, and the partial derivative with respect to the θ direction is used as the known parameter obtained from the n+1 step, thus completing one iteration cycle. After

ISSN: 2710-0588

completing the above iteration cycle, the solution of the n+2 step is used as the initial value of the new nth step, and the next iteration cycle calculation begins. For equation (4), let $Q=\overline{p}^2$, the iterative solution of the first step is as follows:

$$\begin{aligned}&\frac{\overline{h}_{i,j}^{n}}{\overline{p}_{i,j}^{n}}\frac{Q_{i,j}^{n+1}-Q_{i,j}^{n}}{\Delta\tau}+2\overline{p}_{i,j}^{n}\frac{\overline{h}_{i,j}^{n+1}-\overline{h}_{i,j}^{n}}{\Delta\tau}+2\Lambda\frac{Q_{i,j}^{n+1}}{\overline{p}_{i,j}^{n}}\frac{\overline{h}_{i,j+1}^{n}-\overline{h}_{i,j-1}^{n}}{2\Delta\theta}\\&+\Lambda\frac{\overline{h}_{i,j}^{n}}{\overline{p}_{i,j}^{n}}\frac{Q_{i,j+1}^{n+1}-Q_{i,j-1}^{n+1}}{2\Delta\theta}-3\left(\overline{h}_{i,j}^{n}\right)^2\frac{\left(\overline{h}_{i,j+1}^{n}-\overline{h}_{i,j-1}^{n}\right)\left(Q_{i,j+1}^{n+1}-Q_{i,j-1}^{n+1}\right)}{4\Delta\theta^2}\\&-3\left(\overline{h}_{i,j}^{n}\right)^2\frac{\left(\overline{h}_{i+1,j}^{n}-\overline{h}_{i-1,j}^{n}\right)\left(Q_{i+1,j}^{n}-Q_{i-1,j}^{n}\right)}{4\Delta\xi^2}\\&-\left(\overline{h}_{i,j}^{n}\right)^3\frac{Q_{i,j+1}^{n+1}-2Q_{i,j}^{n+1}+Q_{i,j-1}^{n+1}}{\Delta\theta^2}-\left(\overline{h}_{i,j}^{n}\right)^3\frac{Q_{i+1,j}^{n}-2Q_{i,j}^{n}+Q_{i-1,j}^{n}}{\Delta\xi^2}=0\end{aligned}\tag{5}$$

In the first iterative solution step, $Q_{n+1}^{i,j+1},Q_{n+1}^{i,j},Q_{n+1}^{i,j-1}$ is an unknown quantity. The second iterative solution step is as follows:

$$\begin{aligned}&\frac{\overline{h}_{i,j}^{n+1}}{\overline{p}_{i,j}^{n+1}}\frac{Q_{i,j}^{n+2}-Q_{i,j}^{n+1}}{\Delta\tau}+2\overline{p}_{i,j}^{n+1}\frac{\overline{h}_{i,j}^{n+2}-\overline{h}_{i,j}^{n+1}}{\Delta\tau}+2\Lambda\frac{Q_{i,j}^{n+1}}{\overline{p}_{i,j}^{n+1}}\frac{\overline{h}_{i,j+1}^{n+1}-\overline{h}_{i,j-1}^{n+1}}{2\Delta\theta}\\&+\Lambda\frac{\overline{h}_{i,j}^{n+1}}{\overline{p}_{i,j}^{n+1}}\frac{Q_{i,j+1}^{n+1}-Q_{i,j-1}^{n+1}}{2\Delta\theta}-3\left(\overline{h}_{i,j}^{n+1}\right)^2\frac{\left(\overline{h}_{i,j+1}^{n+1}-\overline{h}_{i,j-1}^{n+1}\right)\left(Q_{i,j+1}^{n+1}-Q_{i,j-1}^{n+1}\right)}{4\Delta\theta^2}\\&-3\left(\overline{h}_{i,j}^{n+1}\right)^2\frac{\left(\overline{h}_{i+1,j}^{n+1}-\overline{h}_{i-1,j}^{n+1}\right)\left(Q_{i+1,j}^{n+2}-Q_{i-1,j}^{n+2}\right)}{4\Delta\xi^2}\\&-\left(\overline{h}_{i,j}^{n+1}\right)^3\frac{Q_{i,j+1}^{n+1}-2Q_{i,j}^{n+1}+Q_{i,j-1}^{n+1}}{\Delta\theta^2}-\left(\overline{h}_{i,j}^{n+1}\right)^3\frac{Q_{i+1,j}^{n+2}-2Q_{i,j}^{n+2}+Q_{i-1,j}^{n+2}}{\Delta\xi^2}=0\end{aligned}\tag{6}$$

In the second iteration solution step, $Q_{i+1,j}^{n+2}$, $Q_{i,j}^{n+2}$, $Q_{i-1,j}^{n+2}$ is an unknown quantity.

As can be seen from the solution process in this section, the variable-direction implicit method used for the time term can simultaneously discretize the partial derivatives of pressure with respect to time and the partial derivatives of gas film thickness with respect to time. By substituting equations (5) and (6) with the corresponding boundary conditions, the transient pressure distribution of the radial gas bearing can be obtained. Equations (5) and (6) are nonlinear equations, therefore the variable-direction implicit method is not unconditionally stable. To ensure the stability of the calculation method, the following conditions should be met:

(1) The number of computational nodes in the computational domain is not less than 2;

(2) The time step Δτ is less than 0.01.

In the solution process, an over-relaxation iterative method is used to continuously update and form a corresponding triangular matrix, thereby achieving the solution of the above discrete equations. The transient film force acting on the journal can be obtained by integrating for $\overline{p}(\theta,\xi,\tau)$, as follows:

ISSN: 2710-0588

$$F_x = P_a R^2 \int_0^{2\pi} \int_0^{L/R} \overline{p}(\theta, \xi, \tau) \cos\theta \, d\xi \, d\theta \tag{7}$$

$$F_y = P_a R^2 \int_0^{2\pi} \int_0^{L/R} \overline{p}(\theta, \xi, \tau) \sin\theta \, d\xi \, d\theta \tag{8}$$

2.3. Establishment of the Differential Equations of Motion for the Rotor System

The finite element method is one of the commonly used discretization methods for solving partial differential equations. Its main idea is to divide the structure into a finite number of elements. Each element is a solid with a finite number of degrees of freedom, describing small deformations. By combining these elements, a continuum model with finite degrees of freedom is obtained. This study uses the finite element method to discretize the rotor model, thereby obtaining the dynamic equations of the rotor system.

First, the rotor is discretized axially into a series of beam elements. To describe the rotor's motion in three-dimensional space (considering bending and rotational effects), each node typically contains 4 degrees of freedom (DOF):

$$\mathbf{q}_n = \left[u, v, \theta_x, \theta_y \right]^T \tag{9}$$

Where: u, v: lateral translational displacements of the node center in the X and Y directions, respectively. θx, θy: bending rotations of the node section about the X and Y axes (considering additional angular displacements caused by shear).

Due to the introduction of shear deformation, the lateral displacement of the beam is no longer solely determined by the section rotation. A dimensionless parameter is introduced in the derivation to characterize the effect of shear stiffness:

$$\Phi = \frac{12EI}{GA_s L^2} \tag{10}$$

Where E is the elastic modulus, G is the shear modulus, and As is the effective shear area. The interpolation function is modified to more realistically simulate the deformation hysteresis caused by shear in the stiffness distribution within the element.

Using the Lagrange equation or the principle of virtual work, the element characteristic matrix is obtained through functional variational analysis of kinetic and potential energy:

Element mass matrix [M]e: contains translational inertia and section rotational inertia terms.

Element stiffness matrix [K]e: decomposes the total strain energy into bending energy and shear energy, ultimately obtaining the stiffness matrix of the coupled shear parameters.

Gyro matrix [G]e: This is the core of rotor dynamics. During the derivation, the antisymmetric gyro force matrix related to the rotational speed Ω is extracted by considering the change in angular momentum generated during the precession of the section polar rotational inertia.

Finally, the beam element matrices, disk mass matrix, and nonlinear film force of the gas bearing (obtained through transient solution) are assembled using the "standard finite element superposition method" to obtain the system's overall equation:

$$M\ddot{q} + (C + \Omega G)\dot{q} + Kq = F_{unb} + F_{gas} \tag{11}$$

ISSN: 2710-0588

In this model, Fgas represents the resultant force of the gas film calculated in real time using the transient Reynolds equations, rather than a simple stiffness/damping coefficient. This ensures the ability to capture nonlinear behaviors such as "subsynchronous eddying."

2.4. Prediction-Based Multi-Field Coupled Trajectory Method

To address the "weak" coupled trajectory method in gas bearing rotor dynamics, a prediction-based multi-field coupled trajectory method was developed. As shown in Figure 3, the initial condition is the initial position of the rotor in the bearing at time n, i.e., the initial gas film thickness function is Hn. In the prediction-based multi-field coupled algorithm, the gas film thickness function $H_{forecast}^{n+1}$ at time n+1 is obtained through prediction, The initial value of the variable direction implicit method is then substituted into the ADI algorithm to solve the transient gas lubrication Reynolds equation at time n+1 and obtain the transient pressure distribution within the gas film. The transient pressure distribution Pn+1 is integrated to obtain the transient gas film force acting on the rotor. The rotor dynamic response is then solved using the Newmark method to obtain the shaft center trajectory displacement at time n+1, i.e., the gas film thickness function Hn+1 at time n+1, which is used as the initial value for the next iteration.

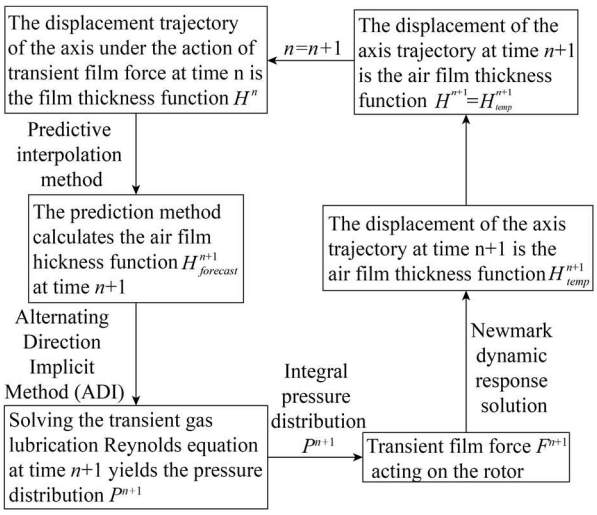

Figure 3. Flowchart of the Predicted Coupled Trajectory Method

Predicting the film thickness function $H_{forecast}^{n+1}$ at time n+1: There are many methods for predicting film thickness, and different methods require different numbers of film thickness functions from previous times. For example, if a linear interpolation method is used, it is assumed that the film thickness function changes linearly with time, as shown in the following equation:

$$\frac{H^{n+1}-H^{n}}{\Delta\tau_{n}}=\frac{H^{n}-H^{n-1}}{\Delta\tau_{n-1}} \tag{12}$$

Therefore, we can conclude that:

$$H^{n+1}=\left(\frac{H^{n}-H^{n-1}}{\Delta\tau_{n-1}}+\frac{H^{n}}{\Delta\tau_{n}}\right)\Delta\tau_{n} \tag{13}$$

ISSN: 2710-0588

As can be seen from equation (13), linear prediction requires the gas film thickness function for the first two time points.

Polynomial interpolation can incorporate more time history information, improving prediction accuracy to some extent. However, when it involves a large number of points, it results in a high-order polynomial, which, while exhibiting high smoothness, lacks convergence and may produce Runge phenomena. Therefore, the order of the polynomial interpolation needs to be carefully selected while considering prediction accuracy.

2.5. Gas Bearing-Rotor Coupled Dynamic Response Algorithm

In summary, this study employs the Newmark method as the analytical method for the dynamic response characteristics of the radial gas bearing-rotor system. First, it is assumed that the acceleration within a time interval is a constant between $\ddot{x}_t$ and $\ddot{x}_{t+\Delta t}$, i.e.:

$$\ddot{x} = \ddot{x}_t + \gamma\left(\ddot{x}_{t+\Delta t} - \ddot{x}_t\right) \tag{14}$$

The first-order Taylor expansion of $\dot{x}_{t+\Delta t}$ with time t as the origin yields:

$$\dot{x}_{t+\Delta t} = \dot{x}_t + \tilde{\ddot{x}}\Delta t \tag{15}$$

Substituting equation (14) into equation (15), we get:

$$\dot{x}_{t+\Delta t} = \dot{x}_t + (1-\gamma)\ddot{x}_t\Delta t + \gamma\ddot{x}_{t+\Delta t}\Delta t \tag{16}$$

Similarly, using the truncated Taylor formula, we can also obtain:

$$x_{t+\Delta t} = x_t + \dot{x}_t\Delta t + \frac{1}{2}\tilde{\ddot{x}}\Delta t^2 \tag{17}$$

By selecting different control parameters δ,

$$\tilde{\ddot{x}} = \ddot{x}_t + 2\delta\left(\ddot{x}_{t+\Delta t} - \ddot{x}\right) \tag{18}$$

Substituting equation (18) into equation (17), we get:

$$x_{t+\Delta t} = x_t + \dot{x}_t\Delta t + (0.5-\delta)\ddot{x}_t\Delta t^2 + \delta\ddot{x}_{t+\Delta t}\Delta t^2 \tag{19}$$

By selecting suitable γ and δ values, and given the displacement vectors x_t, $\dot{x}_t$, and $\ddot{x}_t$ at time t, the response vectors $x_{t+\Delta t}$, $\dot{x}_{t+\Delta t}$, and $\ddot{x}_{t+\Delta t}$ after time Δt can be obtained using the above processing method.

The above process can be used to obtain the rotor dynamic response under transient film force. Since the time step is Δτ in the transient film force solution process, Δτ cannot be used as the time step in the dynamic response solution process in the Newmark numerical integration process. Instead, Δτ is divided into N steps (N=100) to avoid the reduction in accuracy that would occur if Δτ were used directly as the time step in the Newmark numerical integration.

ISSN: 2710-0588

3. System Critical Speed and Stability Boundary Analysis

The schematic diagram of the radial gas bearing-rotor system is shown in Figure 4. This system consists of components such as an elastic shaft segment with distributed mass. The rotor-bearing system is divided into units such as disks and shaft segments along the axis, with each unit connected to the others at nodes. Nodes are selected at the center of the disk, the center of the journal, and some locations along the axis. The entire rotor system is divided into 9 segments with a total of 10 nodes. The radial gas bearings are located at nodes 3 and 8, and the concentrated unbalanced mass acts on node 4. Specific rotor structural parameters are shown in Table 1, and the structural parameters of the radial gas bearing in Figure 4 are shown in Table 2.

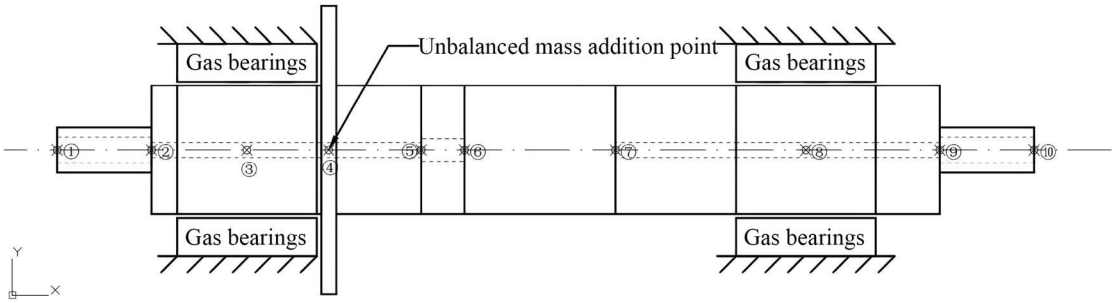

Figure 4. Schematic diagram of the gas dynamic bearing-rotor system.

Table 1. Rotor structural parameters

Name	Value
Rotor length lrotor (m)	0.259
Rotor diameter at bearing Drotor (m)	0.034
Rotor density ρrotor (kg/m3)	7850
Rotor elastic modulus E (GPa)	210

Table 2. Structural parameters of the gas bearing model

Name	Bearing Model 1	Bearing Model 2
Bearing Length l (m)	0.037	0.037
Bearing Diameter D (m)	0.034	0.034
Average Bearing Radius Clearance hm (m)	$30*10^{-6}$	$30*10^{-6}$
Number of Grid Count in Circumferential Direction*NX*	72	72
Number of Grid Count in Half-Length Direction*NZ*	6	6

Accurately determining the critical speed of the rotor assembly during high-speed rotation is crucial for the stable operation of the pneumatic bearing-rotor system. A series of drive speeds were set for the rotor, with each speed differing by 5000 r/min, up to a maximum speed of 160000 r/min. The calculation process involved a total of 33 steps. The critical speeds for the first three forward and reverse precession speeds of the rotor were calculated, and the Campbell's diagram shown in Figure 5 was plotted accordingly.

ISSN: 2710-0588

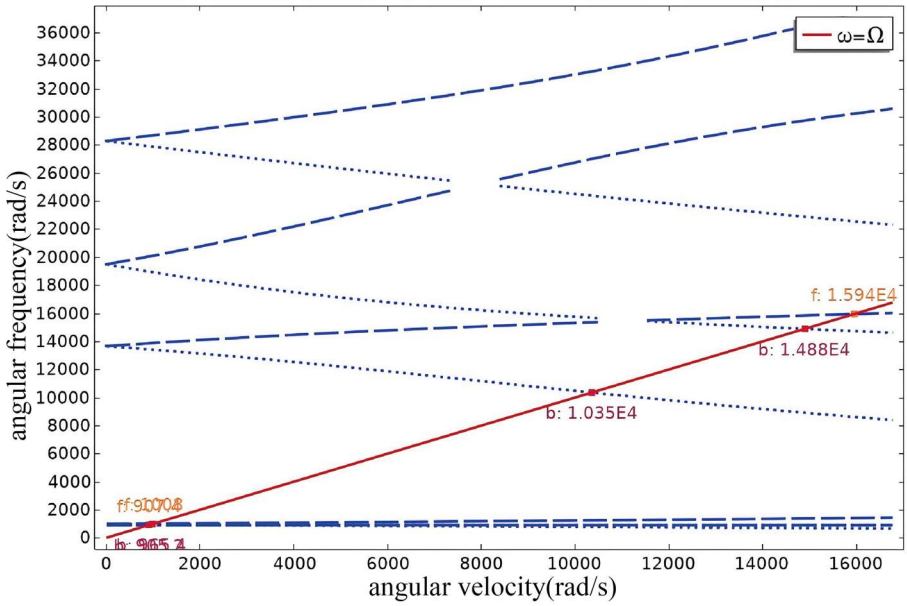

Figure 5. Campbell diagram

Based on the calculation results, the critical speed of the rotor-pneumatic bearing was obtained by analyzing the Campbell diagram. The specific values are listed in Table 3 below.

Table 3. Critical speeds for each order

	Reverse precession (r/min)	Forward precession (r/min)
First-order critical speed	8644	8666
Second-order critical speed	9219	9627
Third-order critical speed	98810	152240

4. Results and Discussion of Nonlinear Dynamic Response

To delve into the nonlinear evolution of the hydrodynamic gas bearing-rotor system under ultra-high-speed operation, this chapter utilizes the fluid-structure interaction transient model established in Chapter 2 to perform a full-spectrum velocity sweep simulation of the system. The analysis focuses on capturing the bifurcation path of the rotor from stable synchronous operation to nonlinear instability and exploring the modulation effect of the nonlinear film force on the system's frequency components.

4.1. Bifurcation Evolution Path of System Motion State

The following discusses the dynamic characteristics of the pure hydrodynamic gas bearing-rotor coupled system with the presence of an eccentric mass. The eccentric mass is applied at node 4, with a magnitude of m1 = 0.115 kg and an eccentricity of e1 = 1e-6 m. The steady-state displacement response of the system in the range of 5000 r/min to 100000 r/min is obtained using the time-stepping method, and the displacement bifurcation diagram in the X direction is extracted, as shown in Figure 6.

As shown in Figure 6, the system exhibits a very clear nonlinear evolution process. In the low-speed range (<11000 r/min), the bifurcation diagram presents a single curve, indicating that the system is in a stable period-1 response state. When the speed increases to the 11000-14000 r/min range, the bifurcation trajectory begins to diverge, indicating that the nonlinear component of the film force begins to challenge the system's damping dissipation capacity. The critical speed occurs at approximately 14000 r/min, at which point the system undergoes Hopf

ISSN: 2710-0588

bifurcation, and the rotor's shaft center trajectory evolves from a small oscillation near the equilibrium point to a large-scale limit cycle motion.

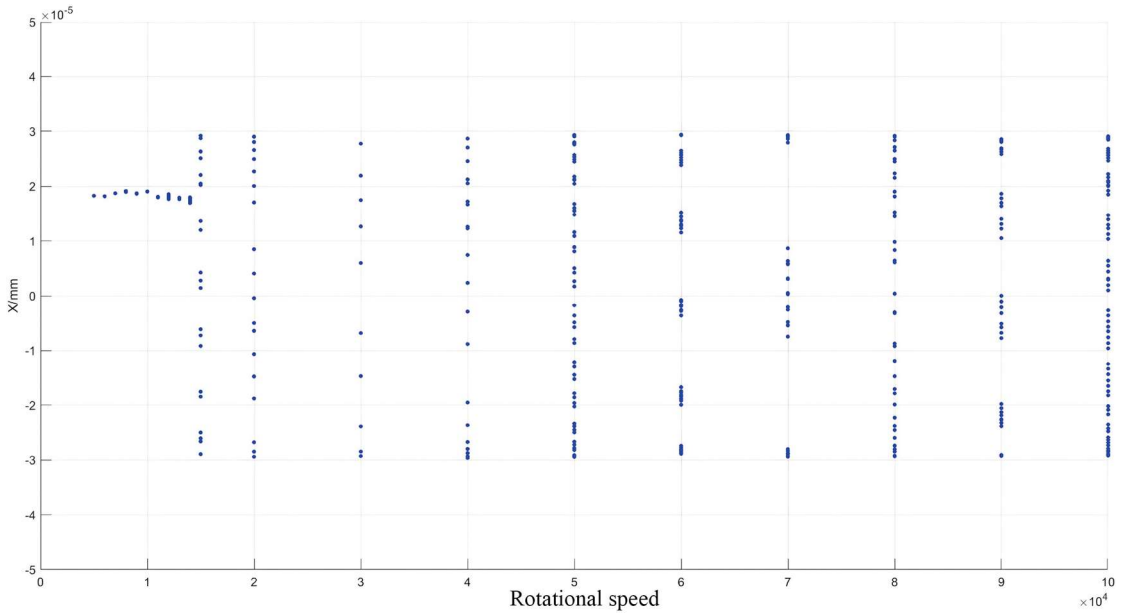

Figure 6. Displacement bifurcation diagram in the X direction

4.2. Transient Characteristic Diagnosis of Typical Motion States

To more intuitively understand the state transitions in the bifurcation diagram, this section selects three representative speed conditions for time-domain, frequency-domain, and phase-space diagnosis.

(1) Periodic Synchronous Response Stage (10,000 r/min)

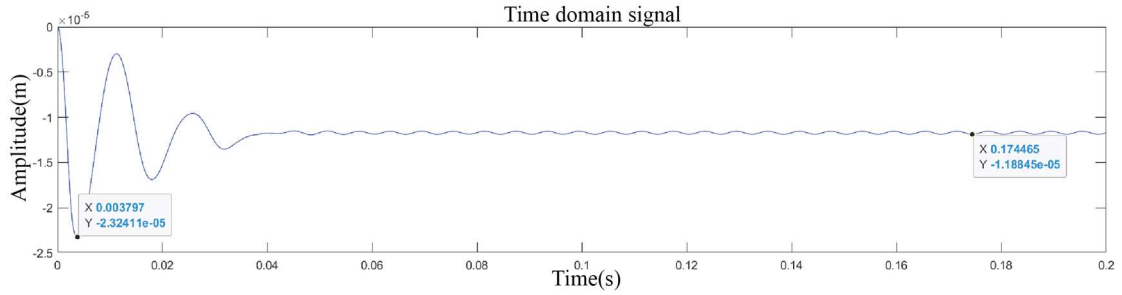

(a)

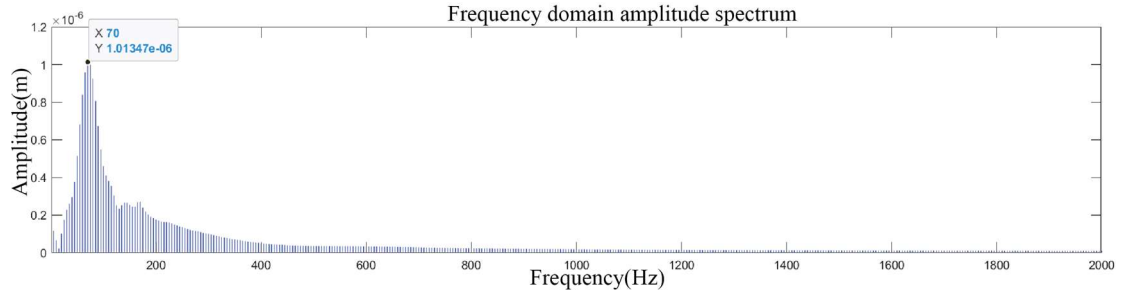

(b)

ISSN: 2710-0588

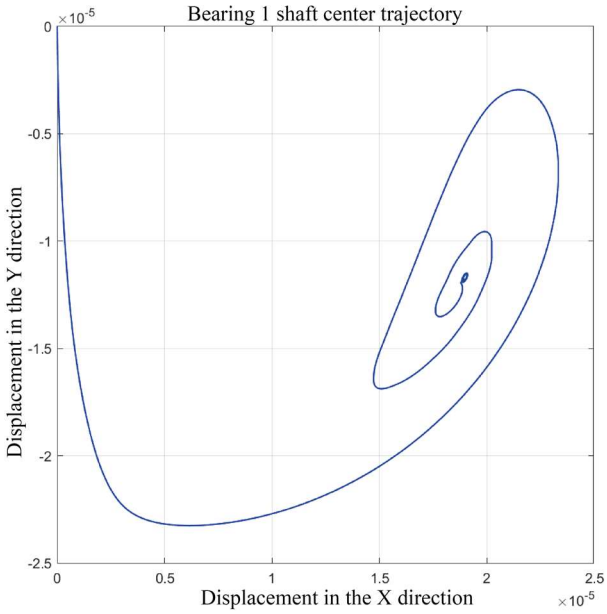

(c)

Figure 7. Time-domain response curve, spectrum, and axis trajectory (10,000 rpm) at node 3, the axis center point.

At this point, the rotational speed is slightly above the first-order critical speed. As shown in Figure 7, the time-domain waveform exhibits standard sinusoidal characteristics, and the axis trajectory converges to a stable ellipse. Spectral analysis shows that the energy is almost entirely concentrated at the first harmonic (1X). This indicates that at 10,000 r/min, although the critical speed has been exceeded, the structural damping provided by the bearing is sufficient to suppress subsynchronous whirl, and the system response is entirely dominated by forced vibrations caused by unbalanced forces.

(2) Instability Criterion and Chaotic Transition (14,055 r/min)

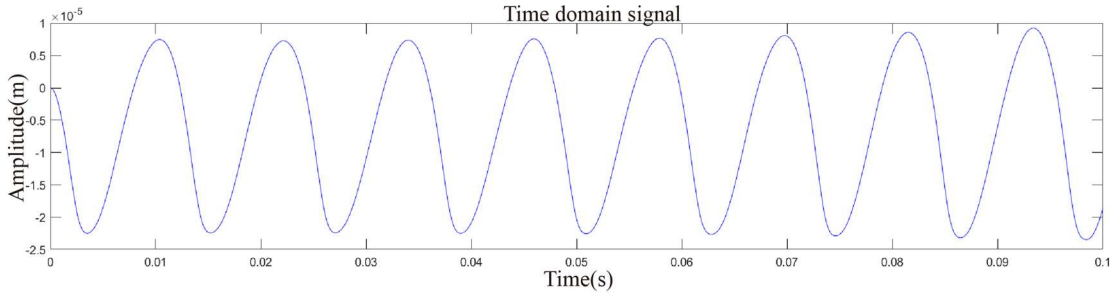

(a)

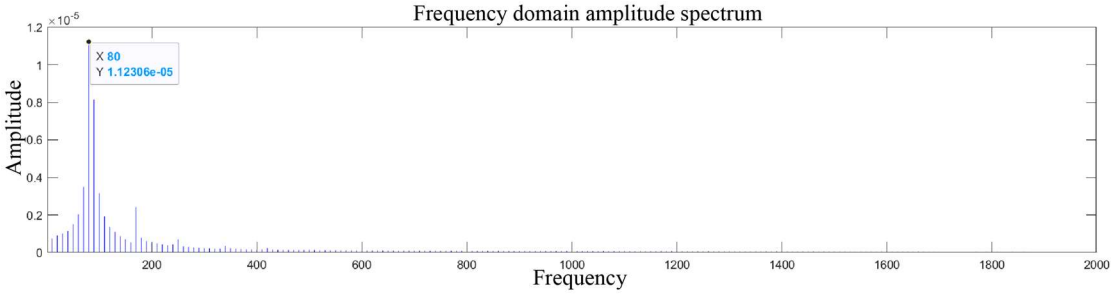

(b)

ISSN: 2710-0588

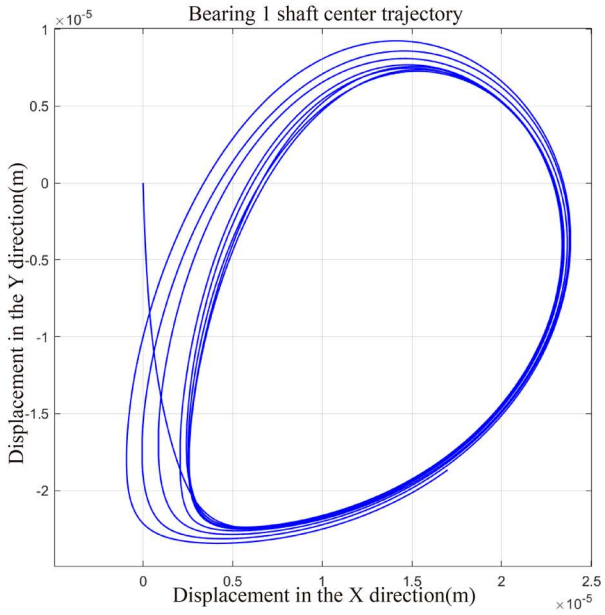

(c)

Figure 8. Time-domain response curve, spectrum, and axis trajectory (14055 rpm) at node 3, the axis center point.

As the rotational speed approaches the instability threshold, the system enters a highly sensitive region. At 14,055 r/min, the rotor exhibits transient chaotic characteristics. A cluster of scattered points on the Poincaré section (Figure 8) indicates that the rotor's trajectory no longer possesses strict periodicity. This chaotic phenomenon is a signal of the system's transition from a stable synchronous response to divergent self-excited vibration, reflecting the strong nonlinear competition between film pressure fluctuations and the rotor's elastic restoring force.

(3) Ultra-high-speed subsynchronous whirl stage (50,000 - 100,000 r/min)

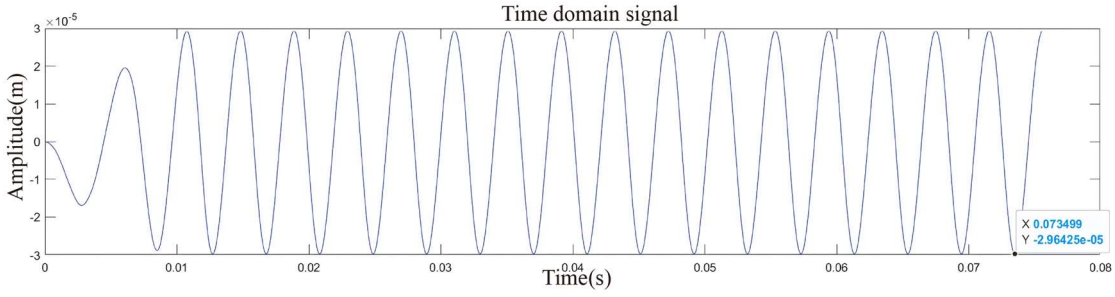

(a)

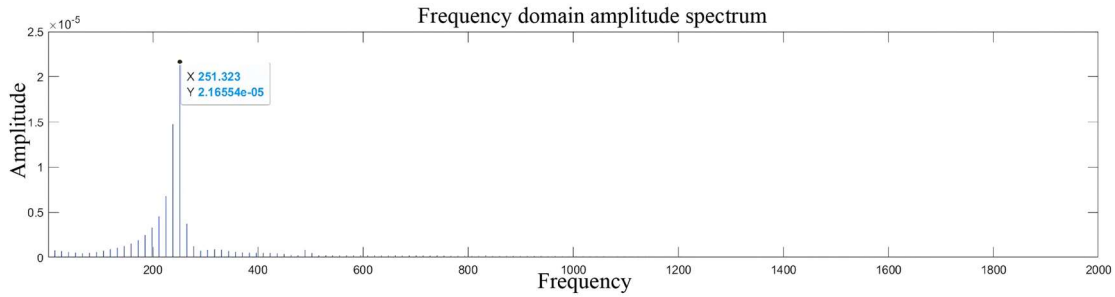

(b)

ISSN: 2710-0588

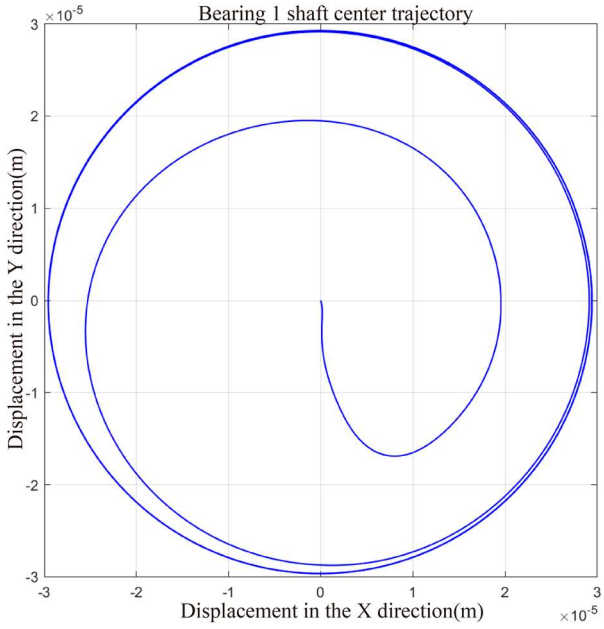

(c)

Figure 9. Time-domain response curve, spectrum, and axis trajectory (50,000 rpm) at node 3, the axis center point.

After crossing the bifurcation point, the system completely enters an unstable state. As shown in Figure 9 (50,000 r/min), the axis trajectory evolves into a huge limiting cycle with an amplitude much greater than that of the low-speed phase. The most significant feature is in the spectrum: in addition to the 1X fundamental frequency, a subsynchronous component with a huge amplitude appears.

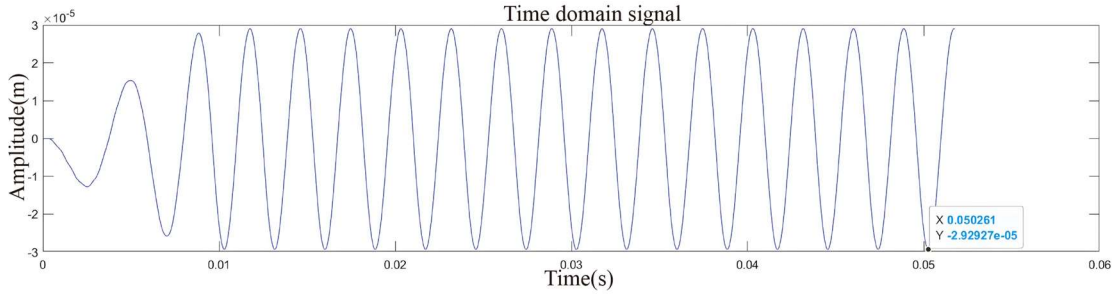

(a)

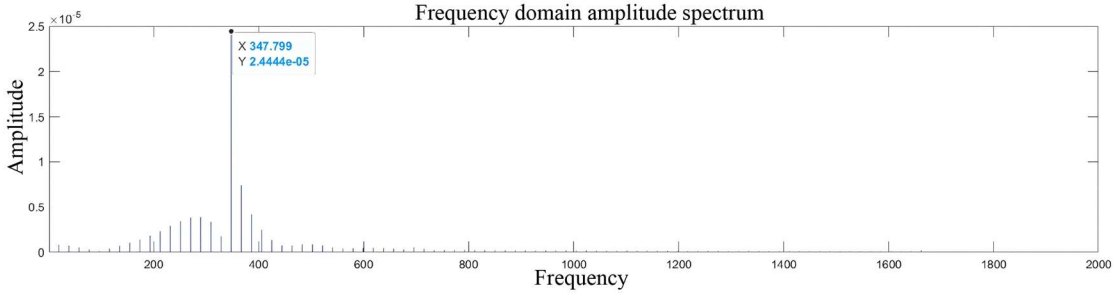

(b)

ISSN: 2710-0588

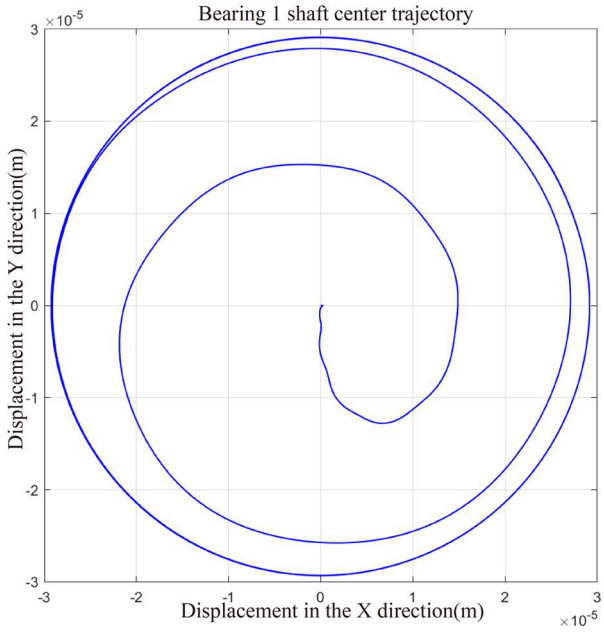

(c)

Figure 10. Time-domain response curve, spectrum, and axis trajectory (100,000 rpm) at node 3, the axis center point.

Frequency Conversion Law: The drift of the subsynchronous whirl frequency deserves further investigation. At 50,000 r/min, the dominant whirl frequency is approximately 0.3X; however, when the speed increases to 100,000 r/min (Figure 10), the whirl frequency further decreases to approximately 0.21X.

Physical Mechanism: This "frequency reduction" phenomenon reflects the softening effect of the gas film at high speeds. As the journal rotation frequency increases drastically, the shear flow velocity of the gas increases, leading to a decrease in the ratio of local gas film stiffness to rotational speed, thus causing the frequency of self-excited vibration to shift to the lower frequency range. This finding has crucial guiding significance for the design of the vibration envelope of high-speed air-bearing rotor systems.

4.3. Summary of Nonlinear Characteristics

Based on the above analysis, the dynamic behavior of this foil bearing-rotor system can be summarized as an evolution from "forced vibration (synchronous)" to "self-excited vibration (subsynchronous limit cycle)". The Hopf bifurcation at 14,000 r/min is a watershed moment for the system's performance. Beyond this speed, although the system can maintain operation through the limit cycle, the huge vibration amplitude will increase the risk of foil wear. Therefore, this bifurcation point is defined as the safe operating limit of the system.

5. Conclusion

This paper establishes a multi-physics coupled nonlinear dynamic model for a dynamic pressure gas foil bearing-high-speed rotor system, considering transient extrusion film force and elastic foil deformation. Through transient numerical simulation and nonlinear diagnosis over a wide speed range, the following main conclusions are drawn:

(1) Effectiveness of the transient multi-field coupled numerical algorithm

The Alternating Direction Implicit (ADI) method combined with the predictive-correction coupled trajectory method successfully solves the problem of nonlinear coupling between the transient Reynolds equation and the rotor motion equation on the time scale. This algorithm,

ISSN: 2710-0588

while ensuring computational accuracy, avoids the limitations of the traditional linear characteristic coefficient method and can capture the evolution of the film pressure field of the rotor during high-speed oscillation in real time. Research shows that introducing the initial value of the predicted displacement in each time step can significantly improve the convergence speed of the nonlinear film force calculation, providing an efficient numerical means for long-term transient simulation of high-speed air-bearing rotor systems.

(2) System nonlinear bifurcation path and instability threshold

The study reveals the typical nonlinear bifurcation law exhibited by the system as the speed increases. In the low-speed range (<11,000 r/min), the system response is dominated by unbalanced excitation, exhibiting stable periodic synchronous motion. When the rotational speed approaches 14,000 r/min, the system undergoes a Hopf bifurcation, and the rotor becomes unstable from a stable equilibrium point, evolving into a divergent stable limit cycle motion. During this process, the Poincaré cross section evolves from a discrete point into a continuous closed loop or a scattered distribution, indicating that the system has undergone a complex evolutionary path from periodic response to chaos, and finally into a divergent stable state. 14,000 r/min can be defined as the dynamic safety boundary of this type of bearing-rotor system.

(3) Frequency Modulation Mechanism of Sub-synchronous Whirl at Ultra-High Speed

Spectral diagnosis of the limit cycle motion reveals that the frequency characteristics of the sub-synchronous whirl exhibit a significant modulation effect with rotational speed. As the rotational speed increases from 15,000 r/min to 100,000 r/min, the duty cycle of the sub-synchronous main frequency is not fixed, but exhibits a nonlinear decay law that gradually decreases from 0.5X to 0.21X. This "frequency shift" phenomenon reflects the redistribution of gas film stiffness saturation and nonlinear restoring force caused by the enhanced gas shear effect under high-speed conditions. This discovery corrects the traditional understanding of "half-frequency eddy" and provides a more accurate theoretical basis for vibration fault diagnosis in ultra-high-speed rotating machinery.

(4) Engineering Guidance Significance

The results of this study indicate that for rotor systems supported by foil hydrodynamic bearings, the design focus should not only be on the critical speed, but also on the amplitude control of the limiting cycle after the instability bifurcation point. By optimizing the stiffness and frictional damping of the foil structure, the occurrence of the Hopf bifurcation point can be effectively delayed or the envelope radius of the limiting cycle can be reduced. The predictive analysis model proposed in this paper can be directly applied to the stability and safety assessment of the support systems of core equipment such as high-speed micro gas turbines and aviation hydrogen liquefaction pumps.

References

[1] Hoffmann R, Liebich R. Characterization and calculation of nonlinear vibrations in gas foil bearing systems–An experimental and numerical investigation[J]. Journal of Sound and Vibration, 2018, 4(12): 389-409.

[2] Block H, Van Rossum J J. The foil bearing a new departure in hydrodynamic lubrication[J]. Journal of Lubrication Engineering, 1953, (9): 316-330.

[3] Andrés L S, Ryu K, Kim T H. Thermal management and rotordynamic performance of a hot rotor-gas foil bearings system. part II: predictions versus test data[J]. Journal of Engineering for Gas Turbine and Power, 2011, 133(6): 062502.1-062502.8.

[4] Ryu K, Kim T H. Prediction of axial and circumferential flow conditions in a high temperature foil bearing with axial cooling flow[J]. Journal of Engineering for Gas Turbine and Power, 2012, 134(9): 094503.1.1-094503-6.

ISSN: 2710-0588

[5] Yu Lie. Aeroelastic lubrication solution of elastic foil bearings [J]. Journal of Xi'an Jiaotong University, 2004, 3: 327-330.

[6] Yu Lie, Qi Shemiao, Geng Haipeng. Complete aeroelastic lubrication solution of elastic foil aerodynamic bearings [J]. Science in China, 2005, 7: 746-760.

[7] Xu Huaijin, Liu Zhansheng, Zhang Guanghui, et al. Characteristics of air film pressure distribution in corrugated foil aerodynamic radial bearings [J]. Bearings, 2008, (6): 23-27.

[8] Xu Huaijin, Liu Zhansheng, Lü Weijian, et al. Dynamic characteristics analysis of gas-lubricated elastic corrugated foil bearings [J]. Journal of Aerospace Power, 2011, 26(5): 1185-1193.